Vietnam Journal of Mechanics, Vol. 47, No. 4 (2025), pp. 340 – 363
DOI: https://doi.org/10.15625/0866-7136/23029

# SIZE-DEPENDENT FREE VIBRATION OF POROUS PIEZOELECTRIC MICROPLATE RESTING ON AN ELASTIC SUBSTRATE USING MSGT, HSDT, AND IGA

**L. T. Phong, P. T. Hung***
*Faculty of Civil Engineering, Ho Chi Minh City University of Technology and Education (HCMUTE), Ho Chi Minh City, Vietnam*
*E-mail: hungpht@hcmute.edu.vn

Received: 13 June 2025 / Revised: 14 August 2025 / Accepted: 05 October 2025
Published online: 05 December 2025

**Abstract.** This work presents the first comprehensive study combining higher-order shear deformation theory (HSDT), modified strain gradient theory (MSGT), and the isogeometric approach (IGA) to investigate the size-dependent free vibration behavior of functionally graded porous piezoelectric (FGPP) microplates. The microplate is composed of a piezoelectric material, with porosity distributed across the thickness following three distinct patterns: symmetric I, symmetric II, and uniform. Hamilton's principle, combined with HSDT and MSGT, is employed to derive the governing equations of the piezoelectric microplate. The natural frequencies of the FGPP microplates are obtained by solving the explicit governing equations using the isogeometric analysis approach. Furthermore, the effects of length scale parameters, porosity distribution patterns, porosity coefficient, external electric voltage, and boundary conditions on the vibrational behavior of the FGPP microplate are thoroughly investigated. The proposed method offers accurate size-dependent predictions and provides new reference solutions for the optimal design of advanced piezoelectric microstructures.

*Keywords*: piezoelectric microplate, isogeometric approach, modified strain gradient theory, higher-order shear deformation theory, elastic foundation.

## 1. INTRODUCTION

Classical plate theories often fail to capture the scale effects observed in microstructures. To address this limitation, various advanced continuum theories, including modified couple stress theory (MCST) and strain gradient theory (MSGT), have been employed to enhance the predictive capability of structural models at the microscale. When

integrated with the constitutive equations of piezoelectric materials, these theories allow for a more precise analysis of the static, dynamic, and stability responses of microstructures under mechanical and electrical loading conditions. Lam et al. [1] were the first to propose the MSGT characterized by three length scale parameters (LSPs) related to higher-order deformation gradients. Compared to single-parameter gradient theories such as MCST [2], MSGT offers greater flexibility in modeling size-dependent behavior by separately capturing different microstructural deformation mechanisms. This improved accuracy, however, has the drawback of requiring the identification of three independent LSPs, which can make experimental calibration more challenging. Zhang et al. [3] investigated the analytical natural frequencies, deflections, and buckling loads of functionally graded (FG) microplates placed on a Winkler–Pasternak foundation based on the refined plate theory (RPT) in conjunction with the MSGT. Kandaz et al. [4] employed the finite element method (FEM) and Euler-Bernoulli theory (EBT) to analyze the static behavior of a gold microbeam, applying both MCST and MSGT. Wang et al. [5] investigated the size effects on the vibration and bending of microplates using the Kirchhoff plate theory (KPT) combined with the MSGT. Utilizing the MSGT, Ansari et al. [6,7] conducted comprehensive analyses of the buckling, bending, and free vibration of FG microplates. Karamanli et al. [8] presented the free vibration of FGP microbeams using the MSGT and quasi-3D theory.

As smart materials, piezoelectric materials possess the ability to bidirectionally convert mechanical and electrical energy owing to their intrinsic electromechanical coupling effect. Owing to this unique property, they have been extensively applied in actuators, sensors, transducers, and energy harvesting devices. In recent years, their applications have expanded to microelectromechanical systems (MEMS), biomedical devices, and precision control systems, where their high sensitivity and rapid response are highly desirable. Wu et al. [9] explored the electromechanical response of FGP shells using higher-order theory. Tanzadeh et al. [10] proposed a finite strip method based on several refined plate theories to analyze the buckling and vibration of piezoelectric laminated composite plates. Huang et al. [11] utilized Von Karman's theory and HSDT to investigate the nonlinear vibrational behavior and dynamic responses of laminated composite plates with FG and piezoelectric layers in a thermal environment. Furthermore, Yan et al. [12] used KPT along with surface piezoelectricity to study the buckling and vibration of piezoelectric nanoplates, including surface effects. Their study showed that the residual surface stress and surface piezoelectricity strongly influence resonant frequencies and buckling loads, especially in thinner nanoplates. Tadi Beni et al. [13] developed a nonlinear model for FG piezoelectric nanobeams using EBT, incorporating mid-plane stretching effects. Ren et al. [14] studied the vibration and buckling of FG piezoelectric nanobeams based on EBT and the differential quadrature method (DQM). Ebrahimi et al. [15] presented an

analytical study on the nonlinear vibration of FG circular sandwich plates with piezoelectric layers under the influence of temperature. Using third-order shear deformation theory (TSDT) and FEM, Phuc et al. [16] investigated the forced and free vibration of FGP plates supported by an elastic foundation. Using the DQM, Ahmed et al. [17] studied the dynamics of an FGPP nanoplate in a thermal environment, applying a nonlocal higher-order plate theory. Wang et al. [18] investigated the static behavior and vibration of FGP plates supported by an elastic foundation, utilizing KPT and DQM. In addition, recent studies have increasingly focused on structures on elastic foundations [19–21].

The IGA was initially developed by Hughes et al. [22], which provides higher-order continuity and smooth derivatives. This property allows IGA to naturally satisfy the continuity requirements of formulations such as the Galerkin weak form of the MSGT, which demands higher-order derivatives. In comparison with meshfree methods, IGA preserves the exact CAD geometry, enables straightforward implementation of boundary conditions, and delivers high computational efficiency for problems that require smooth, higher-order derivatives. Utilizing the MSGT framework, Thai et al. [23] investigated the buckling, bending, and free vibration behaviors of FG microplates using HSDT. In a relevant study, Thai et al. [24] proposed a computational framework combining the MSGT, IGA, and RPT to examine FG microplates. Subsequently, Farzam et al. [25] extended this model to investigate the free vibration characteristics and buckling behavior of FG microplates, considering temperature-dependent material properties. Building upon these developments, Hung et al. [26] applied the same framework to examine the free vibration and mechanical buckling characteristics of metal foam microplates. To the best of the authors' knowledge, no research has yet incorporated MSGT, HSDT, and IGA in a unified framework to explore the free vibration behavior of FGPP microplates. Therefore, this work proposes a numerical model based on the combined use of IGA, MSGT, and HSDT to investigate the vibrational response of FGPP microplates. Particular attention is given to assessing the impacts of geometric parameters, material length scale parameters (LSPs), porosity distribution patterns, porosity gradient patterns, and external electric voltage on the natural frequencies of these microplates.

## 2. THE FUNDAMENTAL EQUATIONS

### 2.1. The material characteristics

This study examines an FGPP microplate with thickness $h$, as illustrated in Fig. 1. The distribution of porosity through the plate thickness is considered uniform and symmetric. The corresponding expressions for the material properties, including elastic coefficients ($c_{ij}$), mass density ($\rho$), piezoelectric coefficients ($e_{ij}$), and dielectric coefficients ($k_{ij}$), associated with these porosity configurations are formulated as follows [17]

$$
\begin{aligned}
&\text{Symmetric I (D-I)} \quad
\begin{cases}
c_{ij} = c_{ij}^{1}\left(1 - e_0 \cos\left(\dfrac{\pi z}{h}\right)\right), \\
\rho = \rho^{1}\left(1 - e_m \cos\left(\dfrac{\pi z}{h}\right)\right), \\
e_{ij} = e_{ij}^{1}\left(1 - e_0 \cos\left(\dfrac{\pi z}{h}\right)\right), \\
k_{ij} = k_{ij}^{1}\left(1 - e_0 \cos\left(\dfrac{\pi z}{h}\right)\right),
\end{cases} \\
&\text{Symmetric II (D-II)} \quad
\begin{cases}
c_{ij} = c_{ij}^{1}\left[1 - e_0^{*}\left(1 - \cos\left(\dfrac{\pi z}{h}\right)\right)\right], \\
\rho = \rho^{1}\left[1 - e_m^{*}\left(1 - \cos\left(\dfrac{\pi z}{h}\right)\right)\right], \\
e_{ij} = e_{ij}^{1}\left[1 - e_0^{*}\left(1 - \cos\left(\dfrac{\pi z}{h}\right)\right)\right], \\
k_{ij} = k_{ij}^{1}\left[1 - e_0^{*}\left(1 - \cos\left(\dfrac{\pi z}{h}\right)\right)\right],
\end{cases} \\
&\text{Uniform (D-III)} \quad
\begin{cases}
c_{ij} = c_{ij}^{1}\zeta_0, \\
\rho = \rho^{1}\zeta_m, \\
e_{ij} = e_{ij}^{1}\zeta_0, \\
k_{ij} = k_{ij}^{1}\zeta_0.
\end{cases}
\end{aligned}
\tag{1}
$$

Here, $c_{ij}^{1}$, $\rho^{1}$, $e_{ij}^{1}$, and $k_{ij}^{1}$ represent the maximum values of elastic coefficients, mass density, piezoelectric coefficients, and dielectric coefficients, respectively. The parameters $e_0$, $e_0^{*}$, and $\zeta_0$ denote the porosity coefficients associated with the D-I, D-II, and D-III configurations, respectively, while $e_m$, $e_m^{*}$, and $\zeta_m$ are referred to as the mass porosity coefficients corresponding to these same configurations. The value of $e_0$ is computed using the following relation

$$
e_0 = 1 - \frac{E_2}{E_1} = 1 - \frac{G_2}{G_1}, \quad 0 < e_0 < 1, \tag{2}
$$

where $E_1, G_1$ and $E_2, G_2$ denote the largest and smallest values of the elastic and shear moduli of the microplate, respectively.

The mass density-Young's modulus relation is taken from Ref. [27] as follows

$$
\rho\left(z\right) = \rho^{1}\sqrt{\frac{E\left(z\right)}{E_1}}. \tag{3}
$$

Substituting Eq. (3) into Eq. (1) yields

$$\begin{cases} 1 - e_m \cos\left(\dfrac{\pi z}{h}\right) = \sqrt{1 - e_0 \cos\left(\dfrac{\pi z}{h}\right)}, \\ 1 - e_m^* \left(1 - \cos\left(\dfrac{\pi z}{h}\right)\right) = \sqrt{1 - e_0^* \left(1 - \cos\left(\dfrac{\pi z}{h}\right)\right)}, \\ \zeta_m = \sqrt{\zeta_0}. \end{cases} \tag{4}$$

Even with varying porosity, the porous microplates retain the same mass, causing

$$\begin{cases} \displaystyle\int_{-h/2}^{h/2} \sqrt{1 - e_0^* \left(1 - \cos\left(\frac{\pi z}{h}\right)\right)} \mathrm{d}z = \int_{-h/2}^{h/2} \sqrt{1 - e_0 \cos\left(\frac{\pi z}{h}\right)} \mathrm{d}z, \\ \displaystyle\int_{-h/2}^{h/2} \sqrt{\zeta_0} \mathrm{d}z = \int_{-h/2}^{h/2} \sqrt{1 - e_0 \cos\left(\frac{\pi z}{h}\right)} \mathrm{d}z. \end{cases} \tag{5}$$

According to Eq. (5), the porosity coefficients $e_0^*$ and $\zeta_0$ corresponding to the initial value of $e_0$ are expressed in Table 1.

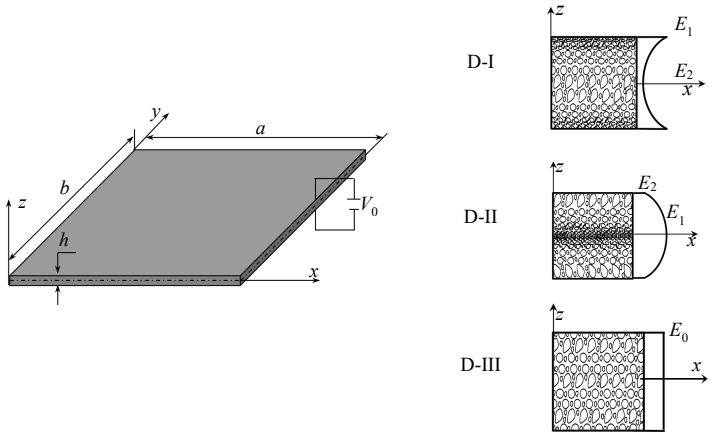


*Fig. 1.* The FGP piezoelectric microplates with various porosity distributions

*Table 1.* The values of porosity coefficients assigned to each porosity distribution type

| $e_0$ | $e_0^*$ | $\zeta_0$ |
|---|---|---|
| 0.1 | 0.1738 | 0.9361 |
| 0.2 | 0.3442 | 0.8716 |
| 0.3 | 0.5103 | 0.8064 |
| 0.4 | 0.6708 | 0.7404 |
| 0.5 | 0.8231 | 0.6733 |
| 0.6 | 0.9612 | 0.6047 |

### 2.2. The governing equations

The displacement field of the microplate, based on the higher-order shear deformation theory, is defined as follows

$$\mathbf{u} = \mathbf{u}_1 + z\,\mathbf{u}_2 + f(z)\,\mathbf{u}_3,$$
$$\text{where } \mathbf{u} = \begin{Bmatrix} \breve{u} \\ \breve{v} \\ \breve{w} \end{Bmatrix}, \quad \mathbf{u}_1 = \begin{Bmatrix} u \\ v \\ w \end{Bmatrix}, \quad \mathbf{u}_2 = \begin{Bmatrix} -w_{,x} \\ -w_{,y} \\ 0 \end{Bmatrix}, \quad \mathbf{u}_3 = \begin{Bmatrix} \beta_x \\ \beta_y \\ 0 \end{Bmatrix}, \tag{6}$$

where $u$, $v$, and $w$ represent the displacements of the mid-surface; $\beta_x$ and $\beta_y$ are two rotations; $f(z) = z - \dfrac{4z^3}{3h^2}$ denotes the shape function; and the notation "," indicates differentiation.

The strain tensor can be defined as follows

$$\boldsymbol{\varepsilon} = \begin{Bmatrix} \boldsymbol{\varepsilon}_b \\ \boldsymbol{\gamma} \end{Bmatrix} = \begin{Bmatrix} \boldsymbol{\varepsilon}_1 + z\boldsymbol{\varepsilon}_2 + f(z)\,\boldsymbol{\varepsilon}_3 \\ f'(z)\,\boldsymbol{\varepsilon}_s \end{Bmatrix}, \tag{7}$$

where

$$\boldsymbol{\varepsilon}_b = \begin{Bmatrix} \varepsilon_x \\ \varepsilon_y \\ \gamma_{xy} \end{Bmatrix}, \ \boldsymbol{\varepsilon}_1 = \begin{Bmatrix} u_{,x} \\ v_{,y} \\ u_{,y} + v_{,x} \end{Bmatrix}, \ \boldsymbol{\varepsilon}_2 = -\begin{Bmatrix} w_{,xx} \\ w_{,yy} \\ 2w_{,xy} \end{Bmatrix}, \ \boldsymbol{\varepsilon}_3 = \begin{Bmatrix} \beta_{x,x} \\ \beta_{y,y} \\ \beta_{x,y} + \beta_{y,x} \end{Bmatrix},$$
$$\boldsymbol{\gamma} = \begin{Bmatrix} \gamma_{xz} \\ \gamma_{yz} \end{Bmatrix}, \quad \boldsymbol{\varepsilon}_s = \begin{Bmatrix} \beta_x \\ \beta_y \end{Bmatrix}, \quad f'(z) = \frac{\mathrm{d}f(z)}{\mathrm{d}z}. \tag{8}$$

A mixed cosine and linear variation of the electric potential across the microplate's thickness is adopted to ensure compatibility with Maxwell's equation, given by [28]

$$\Phi(x, y, z) = g(z)\,\varphi(x, y) + \frac{2z}{h} V_0, \tag{9}$$

where $\Phi(x, y, z)$ is the electric potential, $\varphi(x, y)$ denotes the electric potential of the mid-plane, $V_0$ represents the external electric voltage, and $g(z) = -\cos(\pi z/h)$ corresponds to a distribution function.

From Maxwell's equation, the electric field corresponding to Eq. (9) is expressed as follows

$$\mathbf{E} = -\nabla\Phi \quad \text{or} \quad \begin{Bmatrix} E_x \\ E_y \\ E_z \end{Bmatrix} = -\begin{Bmatrix} \Phi_{,x} \\ \Phi_{,y} \\ \Phi_{,z} \end{Bmatrix} = -\begin{Bmatrix} g(z)\,\varphi_{,x} \\ g(z)\,\varphi_{,y} \\ g'(z)\,\varphi + \dfrac{2V_0}{h} \end{Bmatrix}, \tag{10}$$

where $E_x$, $E_y$, and $E_z$ represent the electric field components.

The constitutive relations for the FGPP microplates are described as follows

$$\begin{aligned}\left\{\begin{array}{c}\boldsymbol{\sigma}_b\\ \boldsymbol{\sigma}_s\end{array}\right\}&=\left[\begin{array}{cc}\mathbf{C}_{ub} & \mathbf{0}\\ \mathbf{0} & \mathbf{C}_{us}\end{array}\right]\left\{\begin{array}{c}\boldsymbol{\varepsilon}_b\\ \boldsymbol{\gamma}\end{array}\right\}-\left[\begin{array}{cc}\mathbf{C}_{ueb} & \mathbf{0}\\ \mathbf{0} & \mathbf{C}_{ues}\end{array}\right]\left\{\begin{array}{c}\mathbf{E}_b\\ \mathbf{E}_s\end{array}\right\},\\ \left\{\begin{array}{c}\mathbf{D}_b\\ \mathbf{D}_s\end{array}\right\}&=\left[\begin{array}{cc}\mathbf{C}_{ueb}^T & \mathbf{0}\\ \mathbf{0} & \mathbf{C}_{ues}^T\end{array}\right]\left\{\begin{array}{c}\boldsymbol{\varepsilon}_b\\ \boldsymbol{\gamma}\end{array}\right\}+\left[\begin{array}{cc}\mathbf{C}_{eb} & \mathbf{0}\\ \mathbf{0} & \mathbf{C}_{es}\end{array}\right]\left\{\begin{array}{c}\mathbf{E}_b\\ \mathbf{E}_s\end{array}\right\},\end{aligned} \tag{11}$$

where

$$\begin{aligned}&\boldsymbol{\sigma}_b=\left\{\begin{array}{c}\sigma_x\\ \sigma_y\\ \tau_{xy}\end{array}\right\},\quad \boldsymbol{\sigma}_s=\left\{\begin{array}{c}\tau_{xz}\\ \tau_{yz}\end{array}\right\},\quad \mathbf{D}_b=\left\{\begin{array}{c}0\\ 0\\ D_z\end{array}\right\},\quad \mathbf{D}_s=\left\{\begin{array}{c}D_x\\ D_y\end{array}\right\},\\ &\mathbf{E}_b=\left\{\begin{array}{c}0\\ 0\\ E_z\end{array}\right\},\quad \mathbf{E}_s=\left\{\begin{array}{c}E_x\\ E_y\end{array}\right\},\quad \mathbf{C}_{ub}=\left[\begin{array}{ccc}\widehat{c}_{11} & \widehat{c}_{12} & 0\\ \widehat{c}_{12} & \widehat{c}_{22} & 0\\ 0 & 0 & \widehat{c}_{66}\end{array}\right],\\ &\mathbf{C}_{ueb}=\left[\begin{array}{ccc}0 & 0 & \widehat{e}_{31}\\ 0 & 0 & \widehat{e}_{31}\\ 0 & 0 & 0\end{array}\right],\quad \mathbf{C}_{us}=\left[\begin{array}{cc}\widehat{c}_{55} & 0\\ 0 & \widehat{c}_{44}\end{array}\right],\quad \mathbf{C}_{ues}=\left[\begin{array}{cc}\widehat{e}_{15} & 0\\ 0 & \widehat{e}_{15}\end{array}\right],\\ &\mathbf{C}_{eb}=\left[\begin{array}{ccc}0 & 0 & 0\\ 0 & 0 & 0\\ 0 & 0 & \widehat{k}_{33}\end{array}\right],\quad \mathbf{C}_{es}=\left[\begin{array}{cc}\widehat{k}_{11} & 0\\ 0 & \widehat{k}_{22}\end{array}\right],\end{aligned} \tag{12}$$

where $\sigma_x$, $\sigma_y$, $\tau_{xy}$, $\tau_{xz}$, and $\tau_{yz}$ represent the stress components; $D_x$, $D_y$ and $D_z$ denote the electric displacements; $\widehat{c}_{ij}$, $\widehat{k}_{ij}$, and $\widehat{e}_{ij}$ are the reduced elastic, dielectric, and piezoelectric coefficients, respectively. The expressions for the reduced coefficients $\widehat{c}_{ij}$, $\widehat{e}_{ij}$, and $\widehat{k}_{ij}$ are presented as follows

$$\begin{aligned}&\widehat{c}_{11}=c_{11}-\frac{c_{13}^2}{c_{33}},\quad \widehat{c}_{12}=c_{12}-\frac{c_{13}^2}{c_{33}},\quad \widehat{c}_{66}=c_{66},\quad \widehat{c}_{55}=c_{55},\quad \widehat{c}_{44}=c_{44},\\ &\widehat{e}_{31}=e_{31}-\frac{e_{33}c_{13}}{c_{33}},\quad \widehat{e}_{15}=e_{15},\quad \widehat{k}_{33}=k_{33}+\frac{e_{33}^2}{c_{33}},\quad \widehat{k}_{11}=k_{11}.\end{aligned} \tag{13}$$

The following variational principle characterizes the free vibration of the FGPP microplate

$$\delta U-\delta K-\delta W_e-\delta W_f=0, \tag{14}$$

where $U$ denote the strain energy, $K$ represents the kinetic energy, $W_e$ and $W_f$ denote the work done by the external electric voltage and elastic foundation, respectively.

The variation of kinetic energy is presented as follows

$$\delta K=-\int_{\Omega}\delta\bar{\mathbf{u}}^T\mathbf{m}_\rho\ddot{\mathbf{u}}\mathrm{d}\Omega, \tag{15}$$

where

$$\bar{\mathbf{u}} = \left\{ \begin{array}{c} \mathbf{u}_1 \\ \mathbf{u}_2 \\ \mathbf{u}_3 \end{array} \right\}, \quad \mathbf{m}_\rho = \left[ \begin{array}{ccc} \mathbf{I}_0 & \mathbf{0} & \mathbf{0} \\ \mathbf{0} & \mathbf{I}_0 & \mathbf{0} \\ \mathbf{0} & \mathbf{0} & \mathbf{I}_0 \end{array} \right], \quad \mathbf{I}_0 = \left[ \begin{array}{ccc} I_1 & I_2 & I_4 \\ I_2 & I_3 & I_5 \\ I_4 & I_5 & I_6 \end{array} \right],$$
$$(I_1, I_2, I_3, I_4, I_5, I_6) = \int_{-h/2}^{h/2} \left(1, z, z^2, f(z), zf(z), (f(z))^2\right) \rho(z)\, \mathrm{d}z. \tag{16}$$

Using the MSGT [1], the virtual strain energy associated with the FGPP microplate is represented as follows

$$\delta U = \int_V \left( \delta \boldsymbol{\varepsilon}_b^T \boldsymbol{\sigma}_b + \delta \boldsymbol{\gamma}^T \boldsymbol{\sigma}_s - \delta \mathbf{E}_b^T \mathbf{D}_b - \delta \mathbf{E}_s^T \mathbf{D}_s + \delta \boldsymbol{\chi}^T \mathbf{m} + \delta \boldsymbol{\zeta}^T \mathbf{p} + \delta \boldsymbol{\eta}^T \mathbf{q} \right) \mathrm{d}V. \tag{17}$$

Here, $\boldsymbol{\zeta}$, $\boldsymbol{\chi}$, and $\boldsymbol{\eta}$ denote the dilatation gradient vector, the rotation gradient tensor, and the deviatoric stretch gradient tensor, respectively, while the associated tensors of higher-order stress are denoted by $\mathbf{m}$, $\mathbf{p}$, and $\mathbf{q}$.

The definition for tensors $\boldsymbol{\chi}$, $\boldsymbol{\zeta}$, and $\boldsymbol{\eta}$ can be stated as

$$\begin{aligned}
\boldsymbol{\chi} &= \left\{ \begin{array}{c} \boldsymbol{\chi}_b \\ \boldsymbol{\chi}_s \end{array} \right\}, \quad \boldsymbol{\chi}_b = \left\{ \begin{array}{c} \chi_{xx} \\ \chi_{yy} \\ \chi_{xy} \\ \chi_{zz} \end{array} \right\} = \boldsymbol{\chi}_{1b} + f'(z)\, \boldsymbol{\chi}_{2b}, \\
\boldsymbol{\chi}_s &= \left\{ \begin{array}{c} \chi_{xz} \\ \chi_{yz} \end{array} \right\} = \boldsymbol{\chi}_{1s} + f(z)\, \boldsymbol{\chi}_{2s} + f''(z)\, \boldsymbol{\chi}_{3s}, \\
\boldsymbol{\zeta} &= \left\{ \begin{array}{c} \zeta_x \\ \zeta_y \\ \zeta_z \end{array} \right\} = \boldsymbol{\zeta}_1 + z\boldsymbol{\zeta}_2 + f(z)\, \boldsymbol{\zeta}_3 + f'(z)\, \boldsymbol{\zeta}_4, \\
\boldsymbol{\eta} &= \left\{ \begin{array}{c} \boldsymbol{\eta}_b \\ \boldsymbol{\eta}_s \end{array} \right\}, \quad \boldsymbol{\eta}_b = \left\{ \begin{array}{c} \eta_{xxx} \\ \eta_{yyy} \\ \eta_{yyx} \\ \eta_{xxy} \\ \eta_{zzx} \\ \eta_{zzy} \end{array} \right\} = \boldsymbol{\eta}_{1b} + z\boldsymbol{\eta}_{2b} + f(z)\, \boldsymbol{\eta}_{3b} + f''(z)\, \boldsymbol{\eta}_{4b}, \\
\boldsymbol{\eta}_s &= \left\{ \begin{array}{c} \eta_{zzz} \\ \eta_{xxz} \\ \eta_{yyz} \\ \eta_{xyz} \end{array} \right\} = \boldsymbol{\eta}_{1s} + f'(z)\, \boldsymbol{\eta}_{2s},
\end{aligned} \tag{18}$$

where

$$\boldsymbol{\chi}_{1b}=\frac{1}{2}\begin{Bmatrix}2w_{,xy}\\-2w_{,xy}\\w_{,yy}-w_{,xx}\\0\end{Bmatrix},\quad \boldsymbol{\chi}_{2b}=\frac{1}{4}\begin{Bmatrix}-2\beta_{y,x}\\2\beta_{x,y}\\\beta_{x,x}-\beta_{y,y}\\2\left(\beta_{y,x}-\beta_{x,y}\right)\end{Bmatrix},\quad \boldsymbol{\chi}_{1s}=\begin{Bmatrix}\frac{1}{4}\left(v_{,xx}-u_{,xy}\right)\\\frac{1}{4}\left(v_{,xy}-u_{,yy}\right)\end{Bmatrix},$$

$$\boldsymbol{\chi}_{2s}=\begin{Bmatrix}\frac{1}{4}\left(\beta_{y,xx}-\beta_{x,xy}\right)\\\frac{1}{4}\left(\beta_{y,xy}-\beta_{x,yy}\right)\end{Bmatrix},\quad \boldsymbol{\chi}_{3s}=-\begin{Bmatrix}\frac{\beta_y}{4}\\\frac{-\beta_x}{4}\end{Bmatrix},\quad \boldsymbol{\zeta}_1=\begin{Bmatrix}u_{,xx}+v_{,xy}\\v_{,yy}+u_{,xy}\\-\left(w_{,xx}+w_{,yy}\right)\end{Bmatrix},$$

$$\boldsymbol{\zeta}_2=-\begin{Bmatrix}w_{,xxx}+w_{,xyy}\\w_{,yyy}+w_{,xxy}\\0\end{Bmatrix},\quad \boldsymbol{\zeta}_3=\begin{Bmatrix}\beta_{x,xx}+\beta_{y,xy}\\\beta_{x,xy}+\beta_{y,yy}\\0\end{Bmatrix},\quad \boldsymbol{\zeta}_4=\begin{Bmatrix}0\\0\\\beta_{x,x}+\beta_{y,y}\end{Bmatrix},$$

$$\boldsymbol{\eta}_{1b}=\frac{1}{15}\begin{Bmatrix}6u_{,xx}-3u_{,yy}-6v_{,xy}\\6v_{,yy}-3v_{,xx}-6u_{,xy}\\-3u_{,xx}+4u_{,yy}+8v_{,xy}\\-3v_{,yy}+4v_{,xx}+8u_{,xy}\\-3u_{,xx}-u_{,yy}-2v_{,xy}\\-3v_{,yy}-v_{,xx}-2u_{,xy}\end{Bmatrix},\quad \boldsymbol{\eta}_{2b}=\frac{1}{5}\begin{Bmatrix}-2w_{,xxx}+3w_{,xyy}\\-2w_{,yyy}+3w_{,xxy}\\w_{,xxx}-4w_{,xyy}\\w_{,yyy}-4w_{,xxy}\\w_{,xxx}+w_{,xyy}\\w_{,yyy}+w_{,xxy}\end{Bmatrix},$$

$$\boldsymbol{\eta}_{3b}=\frac{1}{15}\begin{Bmatrix}6\beta_{x,xx}-3\beta_{x,yy}-6\beta_{y,xy}\\6\beta_{y,yy}-3\beta_{y,xx}-6\beta_{x,xy}\\3\beta_{x,xx}+5\beta_{x,yy}+8\beta_{y,xy}\\\beta_{y,yy}+4\beta_{y,xx}+8\beta_{x,xy}\\-3\beta_{x,xx}-\beta_{x,yy}-2\beta_{y,xy}\\-3\beta_{y,yy}-\beta_{y,xx}-2\beta_{x,xy}\end{Bmatrix},\quad \boldsymbol{\eta}_{4b}=\frac{1}{15}\begin{Bmatrix}-3\beta_x\\-3\beta_y\\-\beta_x\\-\beta_y\\4\beta_x\\4\beta_y\end{Bmatrix},$$

$$\boldsymbol{\eta}_{1s}=\frac{1}{15}\begin{Bmatrix}3w_{,xx}+3w_{,yy}\\-4w_{,xx}+w_{,yy}\\-4w_{,yy}+w_{,xx}\\-5w_{,xy}\end{Bmatrix},\quad \boldsymbol{\eta}_{2s}=\frac{1}{15}\begin{Bmatrix}-6\beta_{x,x}-6\beta_{y,y}\\8\beta_{x,x}-2\beta_{y,y}\\8\beta_{y,y}-2\beta_{x,x}\\5\beta_{x,y}+5\beta_{y,x}\end{Bmatrix}. \tag{19}$$

As per the MSGT [1], the correlation between higher-order strain measures and corresponding stress tensors is given by

$$\begin{cases}\mathbf{m}_b=2\mu l_1^2\mathbf{I}_{4\times4}\boldsymbol{\chi}_b,\quad \mathbf{m}_s=2\mu l_1^2\mathbf{I}_{2\times2}\boldsymbol{\chi}_s,\\ \mathbf{p}=2\mu l_2^2\mathbf{I}_{3\times3}\boldsymbol{\zeta},\\ \mathbf{q}_b=2\mu l_3^2\mathbf{I}_{6\times6}\boldsymbol{\eta}_b,\quad \mathbf{q}_s=2\mu l_3^2\mathbf{I}_{4\times4}\boldsymbol{\eta}_s,\end{cases} \tag{20}$$

where the identity matrices of dimensions $2\times2, 3\times3, 4\times4$, and $6\times6$ are denoted by $\mathbf{I}_{2\times2}, \mathbf{I}_{3\times3}, \mathbf{I}_{4\times4}$ and $\mathbf{I}_{6\times6}$, respectively; $\mu=\dfrac{\widehat{c}_{44}+\widehat{c}_{55}+\widehat{c}_{66}}{3}$ is Lamé's coefficient; $l_1, l_2$, and $l_3$ indicate three LSPs. And

$$\mathbf{m}=\left\{\begin{array}{c}\mathbf{m}_b\\ \mathbf{m}_s\end{array}\right\},\quad \mathbf{m}_b=\left\{\begin{array}{c}m_{xx}\\ m_{yy}\\ m_{xy}\\ m_{zz}\end{array}\right\},\quad \mathbf{m}_s=\left\{\begin{array}{c}m_{xz}\\ m_{yz}\end{array}\right\},$$
$$\mathbf{p}=\left\{\begin{array}{c}p_x\\ p_y\\ p_z\end{array}\right\},\quad \mathbf{q}=\left\{\begin{array}{c}\mathbf{q}_b\\ \mathbf{q}_s\end{array}\right\},\quad \mathbf{q}_b=\left\{\begin{array}{c}q_{xxx}\\ q_{yyy}\\ q_{yyx}\\ q_{xxy}\\ q_{zzx}\\ q_{zzy}\end{array}\right\},\quad \mathbf{q}_s=\left\{\begin{array}{c}q_{zzz}\\ q_{xxz}\\ q_{yyz}\\ q_{xyz}\end{array}\right\}. \tag{21}$$

Substituting Eqs. (11), (18) into Eq. (17), the variation of the strain energy is reformed by the following expression

$$\begin{aligned}\delta U=&\int_\Omega \delta\bar{\boldsymbol{\varepsilon}}_b^T\left(\mathbf{D}_{ub}\bar{\boldsymbol{\varepsilon}}_b-\mathbf{D}_{ueb}\mathbf{E}_b\right)\mathrm{d}\Omega+\int_\Omega \delta\boldsymbol{\varepsilon}_s^T\left(\mathbf{D}_{us}\boldsymbol{\varepsilon}_s-\mathbf{D}_{ues}\mathbf{E}_s\right)\mathrm{d}\Omega\\&-\int_\Omega \delta\mathbf{E}_b^T\left(\mathbf{D}_{eub}\bar{\boldsymbol{\varepsilon}}_b+\mathbf{D}_{eb}\mathbf{E}_b\right)\mathrm{d}\Omega-\int_\Omega \delta\mathbf{E}_s^T\left(\mathbf{D}_{eus}\boldsymbol{\varepsilon}_s+\mathbf{D}_{es}\mathbf{E}_s\right)\mathrm{d}\Omega\\&+\int_\Omega \delta\bar{\boldsymbol{\chi}}_b^T\bar{\mathbf{D}}_{rb}\bar{\boldsymbol{\Gamma}}_{rb}\bar{\boldsymbol{\chi}}_b\mathrm{d}\Omega+\int_\Omega \delta\bar{\boldsymbol{\chi}}_s^T\bar{\mathbf{D}}_{rs}\bar{\boldsymbol{\Gamma}}_{rs}\bar{\boldsymbol{\chi}}_s\mathrm{d}\Omega+\int_\Omega \delta\bar{\boldsymbol{\zeta}}^T\bar{\mathbf{D}}_{dil}\bar{\boldsymbol{\zeta}}\mathrm{d}\Omega\\&+\int_\Omega \delta\bar{\boldsymbol{\eta}}_b^T\bar{\mathbf{D}}_{deb}\bar{\boldsymbol{\Gamma}}_{deb}\bar{\boldsymbol{\eta}}_b\mathrm{d}\Omega+\int_\Omega \delta\bar{\boldsymbol{\eta}}_s^T\bar{\mathbf{D}}_{des}\bar{\boldsymbol{\Gamma}}_{des}\bar{\boldsymbol{\eta}}_s\mathrm{d}\Omega,\end{aligned} \tag{22}$$

where

$$\bar{\boldsymbol{\varepsilon}}_b=\left\{\begin{array}{c}\varepsilon_1\\ \varepsilon_2\\ \varepsilon_3\end{array}\right\},\quad \mathbf{E}_b=\left\{\begin{array}{c}0\\ 0\\ -\varphi\end{array}\right\},\quad \mathbf{E}_s=\left\{\begin{array}{c}-\varphi_{,x}\\ -\varphi_{,y}\end{array}\right\},\quad \bar{\mathbf{D}}_{ub}=\left[\begin{array}{ccc}\mathbf{A}^b&\mathbf{B}^b&\mathbf{E}^b\\ \mathbf{B}^b&\mathbf{D}^b&\mathbf{F}^b\\ \mathbf{E}^b&\mathbf{F}^b&\mathbf{H}^b\end{array}\right],$$
$$\left(\mathbf{A}^b,\mathbf{B}^b,\mathbf{D}^b,\mathbf{E}^b,\mathbf{F}^b,\mathbf{H}^b\right)=\int_{-h/2}^{h/2}\left(1,z,z^2,f(z),zf(z),(f(z))^2\right)\mathbf{C}_{ub}\mathrm{d}z,$$
$$\mathbf{D}_{us}=\int_{-h/2}^{h/2}\left(f'(z)\right)^2\mathbf{C}_{us}\mathrm{d}z,\quad \mathbf{D}_{ues}=\int_{-h/2}^{h/2}\mathbf{C}_{ues}f'(z)\,g(z)\,\mathrm{d}z,$$
$$\mathbf{D}_{ueb}=\left\{\begin{array}{ccc}\hat{\mathbf{C}}_{ue}^{b1}&\hat{\mathbf{C}}_{ue}^{b2}&\hat{\mathbf{C}}_{ue}^{b3}\end{array}\right\},\quad \left(\hat{\mathbf{C}}_{ue}^{b1},\hat{\mathbf{C}}_{ue}^{b2},\hat{\mathbf{C}}_{ue}^{b3}\right)=\int_{-h/2}^{h/2}\mathbf{C}_{ueb}\left(1,z,f(z)\right)g'(z)\,\mathrm{d}z,$$
$$\mathbf{D}_{eb}=\int_{-h/2}^{h/2}\left(g'(z)\right)^2\mathbf{C}_{eb}\mathrm{d}z,\quad \mathbf{D}_{es}=\int_{-h/2}^{h/2}\left(g(z)\right)^2\mathbf{C}_{es}\mathrm{d}z,\quad \mathbf{D}_{eub}=\mathbf{D}_{ueb}^T,\quad \mathbf{D}_{eus}=\mathbf{D}_{ues}^T, \tag{23}$$

$$\bar{\mathbf{D}}_{rb} = \begin{bmatrix} \mathbf{A}_r^b & \mathbf{B}_r^b \\ \mathbf{B}_r^b & \mathbf{D}_r^b \end{bmatrix}, \quad \bar{\mathbf{D}}_{rs} = \begin{bmatrix} \mathbf{A}_r^s & \mathbf{B}_r^s & \mathbf{E}_r^s \\ \mathbf{B}_r^s & \mathbf{D}_r^s & \mathbf{F}_r^s \\ \mathbf{E}_r^s & \mathbf{F}_r^s & \mathbf{H}_r^s \end{bmatrix}, \quad \bar{\mathbf{D}}_{des} = \begin{bmatrix} \mathbf{A}^{des} & \mathbf{B}^{des} \\ \mathbf{B}^{des} & \mathbf{D}^{des} \end{bmatrix},$$

$$\bar{\mathbf{D}}_{dil} = \begin{bmatrix} \mathbf{A}^{di} & \mathbf{B}^{di} & \mathbf{C}^{di} & \mathbf{E}^{di} \\ \mathbf{B}^{di} & \mathbf{D}^{di} & \mathbf{F}^{di} & \mathbf{L}^{di} \\ \mathbf{C}^{di} & \mathbf{F}^{di} & \mathbf{H}^{di} & \mathbf{O}^{di} \\ \mathbf{E}^{di} & \mathbf{L}^{di} & \mathbf{O}^{di} & \mathbf{P}^{di} \end{bmatrix}, \quad \bar{\mathbf{D}}_{deb} = \begin{bmatrix} \mathbf{A}^{deb} & \mathbf{B}^{deb} & \mathbf{C}^{deb} & \mathbf{E}^{deb} \\ \mathbf{B}^{deb} & \mathbf{D}^{deb} & \mathbf{F}^{deb} & \mathbf{L}^{deb} \\ \mathbf{C}^{deb} & \mathbf{F}^{deb} & \mathbf{H}^{deb} & \mathbf{O}^{deb} \\ \mathbf{E}^{deb} & \mathbf{L}^{deb} & \mathbf{O}^{deb} & \mathbf{P}^{deb} \end{bmatrix},$$

$$\bar{\mathbf{\Gamma}}_{rb} = \begin{bmatrix} \mathbf{\Gamma}_r^b & \mathbf{0} \\ \mathbf{0} & \mathbf{\Gamma}_r^b \end{bmatrix}, \quad \bar{\mathbf{\Gamma}}_{rs} = \begin{bmatrix} \mathbf{\Gamma}_r^s & \mathbf{0} & \mathbf{0} \\ \mathbf{0} & \mathbf{\Gamma}_r^s & \mathbf{0} \\ \mathbf{0} & \mathbf{0} & \mathbf{\Gamma}_r^s \end{bmatrix}, \quad \bar{\mathbf{\Gamma}}_{deb} = \begin{bmatrix} \mathbf{\Gamma}^{deb} & \mathbf{0} & \mathbf{0} & \mathbf{0} \\ \mathbf{0} & \mathbf{\Gamma}^{deb} & \mathbf{0} & \mathbf{0} \\ \mathbf{0} & \mathbf{0} & \mathbf{\Gamma}^{deb} & \mathbf{0} \\ \mathbf{0} & \mathbf{0} & \mathbf{0} & \mathbf{\Gamma}^{deb} \end{bmatrix},$$

$$\bar{\mathbf{\Gamma}}_{des} = \begin{bmatrix} \mathbf{\Gamma}^{des} & \mathbf{0} \\ \mathbf{0} & \mathbf{\Gamma}^{des} \end{bmatrix}, \quad \mathbf{\Gamma}_r^b = diag\,(1,1,2,1), \quad \mathbf{\Gamma}_r^s = diag\,(2,2),$$

$$\mathbf{\Gamma}^{deb} = diag\,(1,1,3,3,3,3), \quad \mathbf{\Gamma}^{des} = diag\,(1,3,3,6),$$

$$\left(\mathbf{A}_r^b, \mathbf{B}_r^b, \mathbf{D}_r^b\right) = 2\int_{-h/2}^{h/2} l_1^2 \left(1, f'(z), \left(f'(z)\right)^2\right) \mu \mathbf{I}_{4\times 4} \mathrm{d}z,$$

$$\left(\mathbf{A}_r^s, \mathbf{B}_r^s, \mathbf{D}_r^s, \mathbf{E}_r^s, \mathbf{F}_r^s, \mathbf{H}_r^s\right) = 2\int_{-h/2}^{h/2} l_1^2 \left(1, f(z), (f(z))^2, f''(z), f(z)f''(z), \left(f''(z)\right)^2\right) \mu \mathbf{I}_{2\times 2} \mathrm{d}z,$$

$$\left(\mathbf{A}^{di}, \mathbf{B}^{di}, \mathbf{D}^{di}, \mathbf{C}^{di}, \mathbf{E}^{di}, \mathbf{F}^{di}\right) = 2\int_{-h/2}^{h/2} l_2^2 \left(1, z, z^2, f(z), f'(z), zf(z)\right) \mu \mathbf{I}_{3\times 3} \mathrm{d}z,$$

$$\left(\mathbf{L}^{di}, \mathbf{H}^{di}, \mathbf{O}^{di}, \mathbf{P}^{di}\right) = 2\int_{-h/2}^{h/2} l_2^2 \left(zf'(z), (f(z))^2, f(z)f'(z), \left(f'(z)\right)^2\right) \mu \mathbf{I}_{3\times 3} \mathrm{d}z,$$

$$\left(\mathbf{A}^{deb}, \mathbf{B}^{deb}, \mathbf{D}^{deb}, \mathbf{C}^{deb}, \mathbf{E}^{deb}, \mathbf{F}^{deb}\right) = 2\int_{-h/2}^{h/2} l_3^2 \left(1, z, z^2, f(z), f''(z), zf(z)\right) \mu \mathbf{I}_{6\times 6} \mathrm{d}z,$$

$$\left(\mathbf{L}^{deb}, \mathbf{H}^{deb}, \mathbf{O}^{deb}, \mathbf{P}^{deb}\right) = 2\int_{-h/2}^{h/2} l_3^2 \left(zf''(z), (f(z))^2, f(z)f''(z), \left(f''(z)\right)^2\right) \mu \mathbf{I}_{6\times 6} \mathrm{d}z,$$

$$\left(\mathbf{A}^{des}, \mathbf{B}^{des}, \mathbf{D}^{des}\right) = 2\int_{-h/2}^{h/2} l_3^2 \left(1, f'(z), \left(f'(z)\right)^2\right) \mu \mathbf{I}_{4\times 4} \mathrm{d}z,$$

where $f''(z) = \dfrac{\mathrm{d}^2 f(z)}{\mathrm{d}z^2}$.

The virtual work performed by the Winkler–Pasternak foundation and external electric voltage are defined as follows

$$\begin{aligned}
&\delta W_e = \int\limits_{\Omega} \delta \mathbf{N}_g^T \mathbf{N}^e \mathbf{N}_g \mathrm{d}\Omega, \quad \mathbf{N}_g = \left\{ \begin{array}{c} w_{,x} \\ w_{,y} \end{array} \right\}, \quad \mathbf{N}^e = 2 \left[ \begin{array}{cc} \widehat{e}_{31} V_0 & 0 \\ 0 & \widehat{e}_{31} V_0 \end{array} \right], \\
&\delta W_f = -\int\limits_{\Omega} \left( k_w w - k_s \nabla^2 w \right) \delta w \mathrm{d}\Omega,
\end{aligned} \tag{24}$$

where $\nabla$ is the gradient operator; $k_s$ and $k_w$ are the shear and spring coefficients of the elastic foundation, respectively.

Inserting the necessary expressions into Eq. (14), the governing equation of the FGPP microplate is described as follows

$$\begin{aligned}
&\int\limits_{\Omega} \delta \bar{\boldsymbol{\varepsilon}}_b^T \left( \mathbf{D}_{ub} \bar{\boldsymbol{\varepsilon}}_b - \mathbf{D}_{ueb} \mathbf{E}_b \right) \mathrm{d}\Omega + \int\limits_{\Omega} \delta \boldsymbol{\varepsilon}_s^T \left( \mathbf{D}_{us} \boldsymbol{\varepsilon}_s - \mathbf{D}_{ues} \mathbf{E}_s \right) \mathrm{d}\Omega \\
&- \int\limits_{\Omega} \delta \mathbf{E}_b^T \left( \mathbf{D}_{eub} \bar{\boldsymbol{\varepsilon}}_b + \mathbf{D}_{eb} \mathbf{E}_b \right) \mathrm{d}\Omega - \int\limits_{\Omega} \delta \mathbf{E}_s^T \left( \mathbf{D}_{eus} \boldsymbol{\varepsilon}_s + \mathbf{D}_{es} \mathbf{E}_s \right) \mathrm{d}\Omega \\
&+ \int\limits_{\Omega} \delta \bar{\boldsymbol{\chi}}_b^T \bar{\mathbf{D}}_{rb} \bar{\boldsymbol{\Gamma}}_{rb} \bar{\boldsymbol{\chi}}_b \mathrm{d}\Omega + \int\limits_{\Omega} \delta \bar{\boldsymbol{\chi}}_s^T \bar{\mathbf{D}}_{rs} \bar{\boldsymbol{\Gamma}}_{rs} \bar{\boldsymbol{\chi}}_s \mathrm{d}\Omega + \int\limits_{\Omega} \delta \bar{\boldsymbol{\zeta}}^T \bar{\mathbf{D}}_{dil} \bar{\boldsymbol{\zeta}} \mathrm{d}\Omega \\
&+ \int\limits_{\Omega} \delta \bar{\boldsymbol{\eta}}_b^T \bar{\mathbf{D}}_{deb} \bar{\boldsymbol{\Gamma}}_{deb} \bar{\boldsymbol{\eta}}_b \mathrm{d}\Omega + \int\limits_{\Omega} \delta \bar{\boldsymbol{\eta}}_s^T \bar{\mathbf{D}}_{des} \bar{\boldsymbol{\Gamma}}_{des} \bar{\boldsymbol{\eta}}_s \mathrm{d}\Omega + \int\limits_{\Omega} \delta \bar{\mathbf{u}}^T \mathbf{m} \ddot{\mathbf{u}} \mathrm{d}\Omega \\
&+ \int\limits_{\Omega} \left( k_w w - k_s \nabla^2 w \right) \delta w \mathrm{d}\Omega - \int\limits_{\Omega} \delta \mathbf{N}_g^T \mathbf{N}^e \mathbf{N}_g \mathrm{d}\Omega = 0.
\end{aligned} \tag{25}$$

### 2.3. Isogeometric approximation

The approximation of electric and displacement fields based on NURBS basis functions is given as follows [29]

$$\begin{aligned}
&\varphi^h(x,y) = \sum_{e=1}^{m \times n} N_e(x,y) \varphi_e, \quad \mathbf{u}^h(x,y) = \sum_{e=1}^{m \times n} \mathbf{N}_e(x,y) \mathbf{d}_e, \\
&\text{where } \mathbf{N}_e(x,y) = \left[ \begin{array}{ccccc} 1 & 0 & 0 & 0 & 0 \\ 0 & 1 & 0 & 0 & 0 \\ 0 & 0 & 1 & 0 & 0 \\ 0 & 0 & 0 & 1 & 0 \\ 0 & 0 & 0 & 0 & 1 \end{array} \right] N_e(x,y), \quad \mathbf{d}_e = \left\{ \begin{array}{c} u_e \\ v_e \\ w_e \\ \beta_{xe} \\ \beta_{ye} \end{array} \right\},
\end{aligned} \tag{26}$$

where NURBS basis functions are symbolized by $N_e(x,y)$.

The electric field and strain tensors in Eq. (23), based on the approximation (26), are reformulated as follows

$$\mathbf{E}_b = \sum_{e=1}^{m\times n} \bar{\mathbf{B}}_{\varphi be}\varphi_e,\ \mathbf{E}_s = \sum_{e=1}^{m\times n} \bar{\mathbf{B}}_{\varphi se}\varphi_e,\ \bar{\boldsymbol{\varepsilon}}_b = \sum_{e=1}^{m\times n} \left\{ \begin{array}{c} \mathbf{B}_{b1e} \\ \mathbf{B}_{b2e} \\ \mathbf{B}_{b3e} \end{array} \right\} \mathbf{d}_e = \sum_{e=1}^{m\times n} \bar{\mathbf{B}}_{be}\mathbf{d}_e,\ \boldsymbol{\varepsilon}_s = \sum_{e=1}^{m\times n} \bar{\mathbf{B}}_{se}\mathbf{d}_e, \tag{27}$$

where

$$\begin{aligned}
&\bar{\mathbf{B}}_{\varphi be} = \left\{ \begin{array}{c} 0 \\ 0 \\ -N_e \end{array} \right\},\quad \bar{\mathbf{B}}_{\varphi se} = \left\{ \begin{array}{c} -N_{e,x} \\ -N_{e,y} \end{array} \right\},\quad \bar{\mathbf{B}}_{b1e} = \left[ \begin{array}{ccccc} N_{e,x} & 0 & 0 & 0 & 0 \\ 0 & N_{e,y} & 0 & 0 & 0 \\ N_{e,y} & N_{e,x} & 0 & 0 & 0 \end{array} \right], \\
&\bar{\mathbf{B}}_{b2e} = -\left[ \begin{array}{ccccc} 0 & 0 & N_{e,xx} & 0 & 0 \\ 0 & 0 & N_{e,yy} & 0 & 0 \\ 0 & 0 & 2N_{e,xy} & 0 & 0 \end{array} \right],\quad \bar{\mathbf{B}}_{b3e} = \left[ \begin{array}{ccccc} 0 & 0 & 0 & N_{e,x} & 0 \\ 0 & 0 & 0 & 0 & N_{e,y} \\ 0 & 0 & 0 & N_{e,y} & N_{e,x} \end{array} \right], \\
&\bar{\mathbf{B}}_{se} = \left[ \begin{array}{ccccc} 0 & 0 & 0 & N_e & 0 \\ 0 & 0 & 0 & 0 & N_e \end{array} \right].
\end{aligned} \tag{28}$$

Similarly, the tensors $\boldsymbol{\chi}$, $\boldsymbol{\zeta}$, and $\boldsymbol{\eta}$ are rewritten using Eq. (26) as follows

$$\begin{aligned}
&\bar{\boldsymbol{\zeta}} = \left\{ \begin{array}{cccc} \zeta_1 & \zeta_2 & \zeta_3 & \zeta_4 \end{array} \right\}^T = \sum_{e=1}^{m\times n} \left\{ \begin{array}{cccc} \mathbf{B}_{1e}^{dil} & \mathbf{B}_{2e}^{dil} & \mathbf{B}_{3e}^{dil} & \mathbf{B}_{4e}^{dil} \end{array} \right\}^T \mathbf{d}_e = \sum_{e=1}^{m\times n} \bar{\mathbf{B}}_e^{dil}\mathbf{d}_e, \\
&\bar{\boldsymbol{\chi}}_b = \left\{ \begin{array}{cc} \boldsymbol{\chi}_{1b} & \boldsymbol{\chi}_{2b} \end{array} \right\}^T = \sum_{e=1}^{m\times n} \left\{ \begin{array}{cc} \mathbf{B}_{re}^{b1} & \mathbf{B}_{re}^{b2} \end{array} \right\}^T \mathbf{d}_e = \sum_{e=1}^{m\times n} \bar{\mathbf{B}}_{rbe}\mathbf{d}_e, \\
&\bar{\boldsymbol{\chi}}_s = \left\{ \begin{array}{ccc} \boldsymbol{\chi}_{1s} & \boldsymbol{\chi}_{2s} & \boldsymbol{\chi}_{3s} \end{array} \right\}^T = \sum_{e=1}^{m\times n} \left\{ \begin{array}{ccc} \mathbf{B}_{re}^{s1} & \mathbf{B}_{re}^{s2} & \mathbf{B}_{re}^{s3} \end{array} \right\}^T \mathbf{d}_e = \sum_{e=1}^{m\times n} \bar{\mathbf{B}}_{rse}\mathbf{d}_e, \\
&\bar{\boldsymbol{\eta}}_b = \left\{ \begin{array}{cccc} \bar{\boldsymbol{\eta}}_{1b} & \bar{\boldsymbol{\eta}}_{2b} & \bar{\boldsymbol{\eta}}_{3b} & \bar{\boldsymbol{\eta}}_{4b} \end{array} \right\}^T = \sum_{e=1}^{m\times n} \left\{ \begin{array}{cccc} \mathbf{B}_{1e}^{deb} & \mathbf{B}_{2e}^{deb} & \mathbf{B}_{3e}^{deb} & \mathbf{B}_{4e}^{deb} \end{array} \right\}^T \mathbf{d}_e = \sum_{e=1}^{m\times n} \bar{\mathbf{B}}_e^{deb}\mathbf{d}_e, \\
&\bar{\boldsymbol{\eta}}_s = \left\{ \begin{array}{cc} \bar{\boldsymbol{\eta}}_{1s} & \bar{\boldsymbol{\eta}}_{2s} \end{array} \right\}^T = \sum_{e=1}^{m\times n} \left\{ \begin{array}{cc} \mathbf{B}_{1e}^{des} & \mathbf{B}_{2e}^{des} \end{array} \right\}^T \mathbf{d}_e = \sum_{e=1}^{m\times n} \bar{\mathbf{B}}_e^{des}\mathbf{d}_e,
\end{aligned} \tag{29}$$

where

$$\begin{aligned}
&\mathbf{B}_{re}^{b1} = \frac{1}{2}\left[ \begin{array}{ccccc} 0 & 0 & N_{e,xy} & 0 & 0 \\ 0 & 0 & -N_{e,xy} & 0 & 0 \\ 0 & 0 & N_{e,yy}-N_{e,xx} & 0 & 0 \\ 0 & 0 & 0 & 0 & 0 \end{array} \right],\ \mathbf{B}_{re}^{b2} = \frac{1}{4}\left[ \begin{array}{ccccc} 0 & 0 & 0 & 0 & -2N_{e,x} \\ 0 & 0 & 0 & 2N_{e,y} & 0 \\ 0 & 0 & 0 & N_{e,x} & -N_{e,y} \\ 0 & 0 & 0 & -2N_{e,y} & 2N_{e,x} \end{array} \right], \\
&\mathbf{B}_{re}^{s1} = \frac{1}{4}\left[ \begin{array}{ccccc} -N_{e,xy} & N_{e,xx} & 0 & 0 & 0 \\ -N_{e,yy} & N_{e,xy} & 0 & 0 & 0 \end{array} \right],\quad \mathbf{B}_{re}^{s2} = \frac{1}{4}\left[ \begin{array}{ccccc} 0 & 0 & 0 & -N_{e,xy} & N_{e,xx} \\ 0 & 0 & 0 & -N_{e,yy} & N_{e,xy} \end{array} \right], \\
&\mathbf{B}_{re}^{s3} = \frac{1}{4}\left[ \begin{array}{ccccc} 0 & 0 & 0 & 0 & -N_{e,y} \\ 0 & 0 & 0 & N_{e,x} & 0 \end{array} \right],\ \mathbf{B}_{1e}^{dil} = \left[ \begin{array}{ccccc} N_{e,xx} & N_{e,xy} & 0 & 0 & 0 \\ N_{e,xy} & N_{e,yy} & 0 & 0 & 0 \\ 0 & 0 & -N_{e,xx}-N_{e,yy} & 0 & 0 \end{array} \right],
\end{aligned} \tag{30}$$

$$\mathbf{B}_{2e}^{dil} = -\begin{bmatrix} 0 & 0 & N_{e,xxx}+N_{e,xyy} & 0 & 0 \\ 0 & 0 & N_{e,yyy}+N_{e,xxy} & 0 & 0 \\ 0 & 0 & 0 & 0 & 0 \end{bmatrix}, \quad \mathbf{B}_{3e}^{dil} = \begin{bmatrix} 0 & 0 & 0 & N_{e,xx} & N_{e,xy} \\ 0 & 0 & 0 & N_{e,xy} & N_{e,yy} \\ 0 & 0 & 0 & 0 & 0 \end{bmatrix},$$

$$\mathbf{B}_{4e}^{dil} = \begin{bmatrix} 0 & 0 & 0 & 0 & 0 \\ 0 & 0 & 0 & 0 & 0 \\ 0 & 0 & 0 & N_{e,x} & N_{e,y} \end{bmatrix},$$

$$\mathbf{B}_{1e}^{deb} = \frac{1}{15}\begin{bmatrix} 6N_{e,xx}-3N_{e,yy} & -6N_{e,xy} & 0 & 0 & 0 \\ -6N_{e,xy} & 6N_{e,yy}-3N_{e,xx} & 0 & 0 & 0 \\ -3N_{e,xx}+4N_{e,yy} & 8N_{e,xy} & 0 & 0 & 0 \\ 8N_{e,xy} & -3N_{e,yy}+4N_{e,xx} & 0 & 0 & 0 \\ -3N_{e,xx}-N_{e,yy} & -2N_{e,xy} & 0 & 0 & 0 \\ -2N_{e,xy} & -3N_{e,yy}-N_{e,xx} & 0 & 0 & 0 \end{bmatrix},$$

$$\mathbf{B}_{4e}^{deb} = \frac{1}{15}\begin{bmatrix} 0 & 0 & 0 & -3N_e & 0 \\ 0 & 0 & 0 & 0 & -3N_e \\ 0 & 0 & 0 & -N_e & 0 \\ 0 & 0 & 0 & 0 & -N_e \\ 0 & 0 & 0 & 4N_e & 0 \\ 0 & 0 & 0 & 0 & 4N_e \end{bmatrix},$$

$$\mathbf{B}_{1e}^{des} = \frac{1}{15}\begin{bmatrix} 0 & 0 & 3N_{e,xx}+3N_{e,yy} & 0 & 0 \\ 0 & 0 & -4N_{e,xx}+N_{e,yy} & 0 & 0 \\ 0 & 0 & -4N_{e,yy}+N_{e,xx} & 0 & 0 \\ 0 & 0 & -5N_{e,xy} & 0 & 0 \end{bmatrix}, \quad \mathbf{B}_{2e}^{des} = \frac{1}{15}\begin{bmatrix} 0 & 0 & 0 & -6N_{e,x} & -6N_{e,y} \\ 0 & 0 & 0 & 8N_{e,x} & -2N_{e,y} \\ 0 & 0 & 0 & -2N_{e,x} & 8N_{e,y} \\ 0 & 0 & 0 & 5N_{e,y} & 5N_{e,x} \end{bmatrix}.$$

Besides, according to Eq. (26), the vectors $\bar{\mathbf{u}}$ and $\mathbf{N}_g$ take the following form

$$\bar{\mathbf{u}} = \sum_{e=1}^{m\times n} \begin{Bmatrix} \mathbf{N}_{1e} \\ \mathbf{N}_{2e} \\ \mathbf{N}_{3e} \end{Bmatrix} \mathbf{d}_e = \sum_{e=1}^{m\times n} \bar{\mathbf{N}}_e \mathbf{d}_e, \quad \mathbf{N}_g = \sum_{e=1}^{m\times n} \mathbf{B}_{ge}\mathbf{d}_e, \tag{31}$$

where

$$\begin{aligned} \mathbf{N}_{1e} &= \begin{bmatrix} N_e & 0 & 0 & 0 & 0 \\ 0 & N_e & 0 & 0 & 0 \\ 0 & 0 & N_e & 0 & 0 \end{bmatrix}, \quad \mathbf{N}_{2e} = -\begin{bmatrix} 0 & 0 & N_{e,x} & 0 & 0 \\ 0 & 0 & N_{e,y} & 0 & 0 \\ 0 & 0 & 0 & 0 & 0 \end{bmatrix}, \\ \mathbf{N}_{3e} &= \begin{bmatrix} 0 & 0 & 0 & N_e & 0 \\ 0 & 0 & 0 & 0 & N_e \\ 0 & 0 & 0 & 0 & 0 \end{bmatrix}, \quad \mathbf{B}_{ge} = \begin{bmatrix} 0 & 0 & N_{e,x} & 0 & 0 \\ 0 & 0 & N_{e,y} & 0 & 0 \end{bmatrix}. \end{aligned} \tag{32}$$

The weak form describing the vibrational behavior of the FGPP microplate is given by

$$\left(\mathbf{K} - \omega^2 \mathbf{M}\right) \tilde{\mathbf{d}} = 0, \tag{33}$$

where $\mathbf{K}$ and $\mathbf{M}$ denote the global stiffness and mass matrices, respectively, as expressed below

$$
\begin{aligned}
&\mathbf{K} = \mathbf{K}_u - \mathbf{K}_{u\varphi}\mathbf{K}_{\varphi}^{-1}\mathbf{K}_{u\varphi}^{T}, \quad \mathbf{M} = \int_{\Omega} \bar{\mathbf{N}}^{T}\mathbf{m}\bar{\mathbf{N}}\mathrm{d}\Omega, \quad \mathbf{d} = \tilde{\mathbf{d}}\mathrm{e}^{i\omega t},\\
&\mathbf{K}_u = \int_{\Omega} \bar{\mathbf{B}}_b^{T}\bar{\mathbf{D}}_{ub}\bar{\mathbf{B}}_b\mathrm{d}\Omega + \int_{\Omega} \bar{\mathbf{B}}_s^{T}\bar{\mathbf{D}}_{us}\bar{\mathbf{B}}_s\mathrm{d}\Omega + \int_{\Omega} \bar{\mathbf{B}}_{rb}^{T}\bar{\mathbf{D}}_{rb}\bar{\mathbf{\Gamma}}_{rb}\bar{\mathbf{B}}_{rb}\mathrm{d}\Omega + \int_{\Omega} \bar{\mathbf{B}}_{rs}^{T}\bar{\mathbf{D}}_{rs}\bar{\mathbf{\Gamma}}_{rs}\bar{\mathbf{B}}_{rs}\mathrm{d}\Omega\\
&\quad + \int_{\Omega} \left(\bar{\mathbf{B}}^{dil}\right)^{T}\bar{\mathbf{D}}^{dil}\bar{\mathbf{B}}^{dil}\mathrm{d}\Omega + \int_{\Omega} \left(\bar{\mathbf{B}}^{deb}\right)^{T}\bar{\mathbf{D}}_{deb}\bar{\mathbf{\Gamma}}_{deb}\bar{\mathbf{B}}^{deb}\mathrm{d}\Omega + \int_{\Omega} \left(\bar{\mathbf{B}}^{des}\right)^{T}\bar{\mathbf{D}}_{des}\bar{\mathbf{\Gamma}}_{des}\bar{\mathbf{B}}^{des}\mathrm{d}\Omega\\
&\quad + \int_{\Omega} \mathbf{B}_f^{T}\left(k_w\mathbf{B}_f - k_s\nabla^2\mathbf{B}_f\right)\mathrm{d}\Omega - \int_{\Omega} \mathbf{B}_g^{T}\mathbf{N}^{e}\mathbf{B}_g\mathrm{d}\Omega,\\
&\mathbf{K}_{u\varphi} = -\int_{\Omega} \bar{\mathbf{B}}_b^{T}\bar{\mathbf{D}}_{ueb}\bar{\mathbf{B}}_{eb}\mathrm{d}\Omega - \int_{\Omega} \bar{\mathbf{B}}_s^{T}\bar{\mathbf{D}}_{ues}\bar{\mathbf{B}}_{es}\mathrm{d}\Omega,\\
&\mathbf{K}_{\varphi} = -\int_{\Omega} \bar{\mathbf{B}}_{eb}^{T}\bar{\mathbf{D}}_{eb}\bar{\mathbf{B}}_{eb}\mathrm{d}\Omega - \int_{\Omega} \bar{\mathbf{B}}_{es}^{T}\bar{\mathbf{D}}_{es}\bar{\mathbf{B}}_{es}\mathrm{d}\Omega,\\
&\bar{\mathbf{B}}_f = \left\{\begin{array}{ccccc} 0 & 0 & N_e & 0 & 0 \end{array}\right\},
\end{aligned}
\tag{34}
$$

where $\omega$ and $\tilde{\mathbf{d}}$ represent the natural frequency and mode shapes, respectively.

## 3. NUMERICAL RESULTS

Free vibration response of the FGPP microplate with dimensions $a \times b$ and thickness $h$ are analyzed in this subsection. The microplate is made of PZT-4 with material parameters given by ref. [29] and presented in Table 2. In the numerical investigation, all three LSPs are considered the same ($l = l_1 = l_2 = l_3$), following the approach in [1]. Subsequently, the dimensionless parameters for the FGPP microplates are provided as follows

$$
\bar{\omega} = \frac{\omega a^2}{h}\sqrt{\rho_{PZT-4}/E_{PZT-4}}, \quad K_w = \frac{a^4 k_w}{Eh^3}, \quad K_s = \frac{a^2 k_s}{Eh^3}. \tag{35}
$$

The plate edges are subjected to mixed boundary conditions (BCs), including clamped (C) and simply supported (S) types. The BCs are presented as follows

$$
\begin{aligned}
&\text{SSSS:} \quad (v, w, \beta_y)\big|_{x=0,a} = 0, \quad (u, w, \beta_x)\big|_{y=0,b} = 0\\
&\text{CCCC:} \quad (u, v, w, w_{,n}, \beta_x, \beta_y)\big|_{x=0,a;y=0,b} = 0\\
&\text{SCSC:} \quad (v, w, \beta_y)\big|_{x=0,a} = 0, \quad (u, v, w, w_{,n}, \beta_x, \beta_y)\big|_{y=0,b} = 0
\end{aligned}
\tag{36}
$$

To begin with, the free vibration of an FGP piezoelectric plate ($l$ = 0), consisting of PZT-4 and PZT-5H materials with material parameters tabulated in Table 2, is examined to validate the reliability of the present model. The frequency results ($\bar{\omega}$) obtained in this study are compared with the corresponding values reported in [29] based on RPT and

*Table 2.* The material parameters of the FGP piezoelectric plate [29]

| Properties | PZT-4 | PZT-5H |
|---|---|---|
| Elastic coefficients (GPa) | $c_{11} = c_{22} = 138.499$, $c_{12} = 77.371$, $c_{13} = 73.643$, $c_{33} = 114.745$, $c_{55} = 25.6$, $c_{66} = 30.6$ | $c_{11} = c_{22} = 99.201$, $c_{12} = 54.016$, $c_{13} = 50.778$, $c_{33} = 86.856$, $c_{55} = 21.1$, $c_{66} = 22.6$ |
| Piezoelectric coefficients ($\mathrm{Cm}^{-2}$) | $e_{31} = -5.2$, $e_{33} = 15.08$, $e_{15} = 12.72$ | $e_{31} = -7.209$, $e_{33} = 15.118$, $e_{15} = 12.322$ |
| Dielectric coefficients ($10^{-9}\ \mathrm{C}^2\mathrm{m}^{-2}\mathrm{N}^{-1}$) | $k_{11} = 1.306$, $k_{33} = 1.115$ | $k_{11} = 1.53$, $k_{33} = 1.5$ |
| Density ($\mathrm{kgm}^{-3}$) | $\rho = 7600$ | $\rho = 7750$ |

analytical methods for perfect and imperfect FGP piezoelectric plates, and the outcomes are listed in Table 3. Table 3 reveals that the computed results are highly consistent with the published findings. Additionally, a mesh sensitivity analysis is performed using three IGA mesh densities (9×9, 11×11, and 13×13) to evaluate convergence, revealing that the 11×11 mesh achieves an optimal balance between accuracy and computational cost, and is therefore adopted for all subsequent analyses. Next, the free vibration of the metal foam microplate with material parameters are taken from Ref. [30] ($E_1 = 200$ GPa, $\nu_1 = 0.33$, $\rho_1 = 7850\ \mathrm{kg/m}^3$) is examined, and the first normalized frequency $\breve{\omega} = \omega h\sqrt{\rho_1/E_1}$ is presented in Table 4. The results are compared with the corresponding values reported in [30], which were derived using RPT, MSGT, and IGA. As seen in Table 4, the computed results exhibit excellent agreement with the published values. Comparison results in Tables 3 and 4 show that the proposed model provides accurate and consistent results in the investigation of the free vibration behavior of FGPP microplates.

*Table 3.* The lowest normalized frequency of the FGP piezoelectric square plate with different external electric voltage under SSSS boundaries ($a/h = 100$, $l = 0$, $K_w = K_s = 0$)

| $\alpha$ | $V_0$ (V) | Mesh | $p$ | | | | | |
|---|---|---|---|---|---|---|---|---|
| | | | 0.2 | | 1 | | 5 | |
| | | | Present | Ref. [29] | Present | Ref. [29] | Present | Ref. [29] |
| 0 | −500 | 9 × 9 | 6.20649 | 6.20555 | 6.00371 | 6.00294 | 5.85519 | 5.85444 |
| | | 11 × 11 | 6.20648 | | 6.00371 | | 5.85518 | |

| $\alpha$ | $V_0$ (V) | Mesh | $p$ | | | | | |
|---|---|---|---|---|---|---|---|---|
| | | | 0.2 | | 1 | | 5 | |
| | | | Present | Ref. [29] | Present | Ref. [29] | Present | Ref. [29] |
| | | $13 \times 13$ | 6.20648 | | 6.00370 | | 5.85518 | |
| | 0 | $9 \times 9$ | 6.03124 | 6.03027 | 5.81868 | 5.81787 | 5.66199 | 5.66120 |
| | | $11 \times 11$ | 6.03123 | | 5.81867 | | 5.66199 | |
| | | $13 \times 13$ | 6.03123 | | 5.81866 | | 5.66198 | |
| | 500 | $9 \times 9$ | 5.85074 | 5.84974 | 5.62755 | 5.62671 | 5.46197 | 5.46113 |
| | | $11 \times 11$ | 5.85073 | | 5.62755 | | 5.46196 | |
| | | $13 \times 13$ | 5.85073 | | 5.62755 | | 5.46196 | |
| 0.2 | $-500$ | $9 \times 9$ | 6.24911 | 6.24814 | 5.99179 | 5.99103 | 5.80577 | 5.80503 |
| | | $11 \times 11$ | 6.24910 | | 5.99178 | | 5.80576 | |
| | | $13 \times 13$ | 6.24910 | | 5.99178 | | 5.80576 | |
| | 0 | $9 \times 9$ | 6.07613 | 6.07512 | 5.80651 | 5.80571 | 5.61032 | 5.60954 |
| | | $11 \times 11$ | 6.07612 | | 5.80650 | | 5.61031 | |
| | | $13 \times 13$ | 6.07612 | | 5.80650 | | 5.61031 | |
| | 500 | $9 \times 9$ | 5.89807 | 5.89704 | 5.61512 | 5.61429 | 5.40781 | 5.40698 |
| | | $11 \times 11$ | 5.89807 | | 5.61511 | | 5.40781 | |
| | | $13 \times 13$ | 5.89806 | | 5.61511 | | 5.40780 | |

*Table 4.* The first normalized frequency of the metal foam microplate with various length-to-thickness ratios ($e_0 = 0.2$, $a/h = 10$)

| BCs | Porosity distribution | Theory | $l/h$ | | | | |
|---|---|---|---|---|---|---|---|
| | | | 0 | 0.1 | 0.2 | 0.5 | 1 |
| SSSS | Uniform | Present | 0.0562 | 0.0602 | 0.0706 | 0.1206 | 0.2206 |
| | | Ref. [30] | 0.0562 | 0.0601 | 0.0706 | 0.1203 | 0.2196 |
| | Symmetric | Present | 0.0579 | 0.0618 | 0.0721 | 0.1218 | 0.2220 |
| | | Ref. [30] | 0.0579 | 0.0617 | 0.0720 | 0.1215 | 0.2212 |
| | Asymmetric | Present | 0.0565 | 0.0604 | 0.0709 | 0.1209 | 0.2211 |
| | | Ref. [30] | 0.0565 | 0.0604 | 0.0708 | 0.1206 | 0.2202 |
| CCCC | Uniform | Present | 0.0963 | 0.1033 | 0.1220 | 0.2100 | 0.3851 |
| | | Ref. [30] | 0.0971 | 0.1042 | 0.1227 | 0.2102 | 0.3843 |
| | Symmetric | Present | 0.0986 | 0.1056 | 0.1243 | 0.2129 | 0.3898 |
| | | Ref. [30] | 0.0995 | 0.1065 | 0.1250 | 0.2131 | 0.3892 |
| | Asymmetric | Present | 0.0967 | 0.1037 | 0.1224 | 0.2108 | 0.3864 |
| | | Ref. [30] | 0.0976 | 0.1046 | 0.1232 | 0.2109 | 0.3857 |

We now examine the free vibrational response of the FGPP microplates under the impact of the scale-to-thickness ratio, porosity coefficients, porosity distributions, external electric voltage, shear and spring coefficients, and BCs. The lowest six dimensionless natural frequencies ($\bar{\omega}$) of the SSSS and CCCC FGPP microplates, under the impact of the porosity coefficient and porosity distribution, are expressed in Tables 5 and 6, respectively. The results indicate that increasing the porosity coefficient results in a decline in the FGPP microplate's frequencies. The FGPP microplate with a D-I porosity pattern provides the highest frequencies, while the microplate with a D-II porosity pattern provides the lowest. Fig. 2 illustrates the first normalized frequency of the FGPP square microplate under the scale-to-thickness ratio ($l/h$) impact. The findings reveal that increasing the $l/h$ ratio increases the vibrational stiffness of the FGPP microplate. Furthermore, the CCCC configuration produces the highest natural frequencies among the considered boundary conditions, while the SSSS configuration yields the lowest. The impact of the external

*Table 5.* The first six dimensionless natural frequencies of the SSSS FGPP microplates with different porosity coefficients and porosity distributions ($a/h = 10, l/h = 0.1$, $V_0 = -100$ V, $K_w = 2, K_s = 0.1$)

| Porosity distribution | Mode | $e$ | | | | | |
|---|---|---|---|---|---|---|---|
| | | 0.1 | 0.2 | 0.3 | 0.4 | 0.5 | 0.6 |
| D-I | 1 | 6.4754 | 6.4604 | 6.4484 | 6.4404 | 6.4376 | 6.4415 |
| | 2 | 14.9939 | 14.8983 | 14.8000 | 14.6976 | 14.5895 | 14.4723 |
| | 3 | 14.9939 | 14.8983 | 14.8000 | 14.6976 | 14.5895 | 14.4723 |
| | 4 | 23.0037 | 22.8025 | 22.5871 | 22.3529 | 22.0925 | 21.7950 |
| | 5 | 28.0999 | 27.8185 | 27.5134 | 27.1771 | 26.7983 | 26.3598 |
| | 6 | 28.1008 | 27.8194 | 27.5144 | 27.1781 | 26.7993 | 26.3609 |
| D-II | 1 | 6.2871 | 6.0672 | 5.8324 | 5.5826 | 5.3216 | 5.0661 |
| | 2 | 14.5360 | 14.0859 | 13.5152 | 12.8917 | 12.2192 | 11.5343 |
| | 3 | 14.5360 | 14.0859 | 13.5152 | 12.8917 | 12.2192 | 11.5343 |
| | 4 | 22.5070 | 21.7493 | 20.9096 | 19.9776 | 19.3031 | 19.1054 |
| | 5 | 27.5627 | 26.6737 | 25.6802 | 24.5677 | 23.3361 | 22.0492 |
| | 6 | 27.5635 | 26.6744 | 25.6809 | 24.5682 | 23.3364 | 22.0493 |
| D-III | 1 | 6.4068 | 6.3164 | 6.2211 | 6.1202 | 6.0126 | 5.8969 |
| | 2 | 14.8553 | 14.6096 | 14.3479 | 14.0676 | 13.7645 | 13.4325 |
| | 3 | 14.8553 | 14.6096 | 14.3479 | 14.0676 | 13.7645 | 13.4325 |
| | 4 | 22.8280 | 22.4398 | 22.0258 | 21.5816 | 21.0999 | 20.5709 |
| | 5 | 27.9119 | 27.4334 | 26.9229 | 26.3747 | 25.7800 | 25.1262 |
| | 6 | 27.9128 | 27.4343 | 26.9237 | 26.3755 | 25.7808 | 25.1270 |

electric voltage ($V_0$) on the lowest normalized frequency of the FGPP square microplate is examined, and the results are shown in Fig. 3. As depicted, an increase in the electric voltage decreases the FGPP microplate's vibrational frequency. This is attributed to the induced tensile stresses from the applied voltage, which decrease the effective stiffness of the piezoelectric microplate through electromechanical coupling. Fig. 4 plots the variation of the first normalized natural frequency for a uniform FGPP microplate subjected to different elastic foundation spring and shear coefficients. As observed in Fig. 4, as spring and shear coefficients increase, the FGPP microplate's vibrational stiffness also grows. Finally, the influence of the length-to-thickness ratio on the first normalized frequency of the FGPP microplates under various BCs is investigated, and the results are presented in Fig. 5. As seen in Fig. 5, the vibrational stiffness of the FGPP microplate is enhanced when the $a/h$ ratio increases.

*Table 6*. The first six dimensionless natural frequencies of the CCCC FGPP microplates with different porosity coefficients and porosity distributions ($a/h = 10, l/h = 0.1, V_0 = -100$ V, $K_w = 2, K_s = 0.1$)

| Porosity distribution | Mode | $e$ | | | | | |
|---|---|---|---|---|---|---|---|
| | | 0.1 | 0.2 | 0.3 | 0.4 | 0.5 | 0.6 |
| D-I | 1 | 10.8041 | 10.7194 | 10.6298 | 10.5338 | 10.4290 | 10.3120 |
| | 2 | 20.6539 | 20.4150 | 20.1542 | 19.8652 | 19.5390 | 19.1625 |
| | 3 | 20.6539 | 20.4150 | 20.1542 | 19.8652 | 19.5390 | 19.1625 |
| | 4 | 29.1978 | 28.7995 | 28.3611 | 27.8714 | 27.3152 | 26.6707 |
| | 5 | 34.6491 | 34.1296 | 33.5551 | 32.9110 | 32.1773 | 31.3261 |
| | 6 | 34.9201 | 34.4010 | 33.8270 | 33.1832 | 32.4495 | 31.5975 |
| D-II | 1 | 10.5676 | 10.2191 | 9.8347 | 9.4099 | 8.9459 | 8.4669 |
| | 2 | 20.3385 | 19.7369 | 19.0571 | 18.2853 | 17.4169 | 16.4929 |
| | 3 | 20.3385 | 19.7369 | 19.0571 | 18.2853 | 17.4169 | 16.4929 |
| | 4 | 28.8766 | 28.0963 | 27.2006 | 26.1655 | 24.9788 | 23.6943 |
| | 5 | 34.3685 | 33.5006 | 32.4918 | 31.3098 | 29.9360 | 28.4312 |
| | 6 | 34.6254 | 33.7426 | 32.7175 | 31.5181 | 30.1260 | 28.6034 |
| D-III | 1 | 10.7201 | 10.5454 | 10.3597 | 10.1609 | 9.9463 | 9.7115 |
| | 2 | 20.5455 | 20.1955 | 19.8223 | 19.4217 | 18.9873 | 18.5102 |
| | 3 | 20.5455 | 20.1955 | 19.8223 | 19.4217 | 18.9873 | 18.5102 |
| | 4 | 29.0917 | 28.5905 | 28.0555 | 27.4809 | 26.8573 | 26.1714 |
| | 5 | 34.5613 | 33.9633 | 33.3249 | 32.6390 | 31.8943 | 31.0748 |
| | 6 | 34.8272 | 34.2243 | 33.5807 | 32.8891 | 32.1382 | 31.3119 |

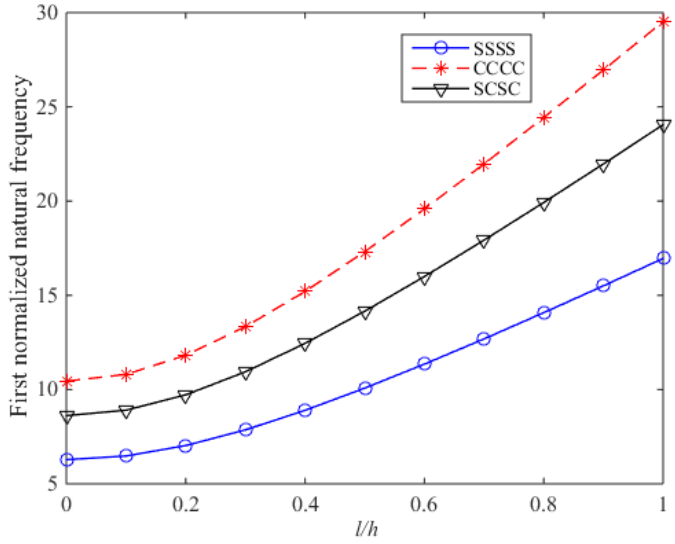


*Fig. 2.* The influence of the scale-to-thickness ratio on the lowest non-dimensional vibrational frequency of the FGPP microplates with various BCs (D-I, $a/h = 10, e_0 = 0.1, V_0 = 100$ V, $K_w = 2, K_s = 0.1$)

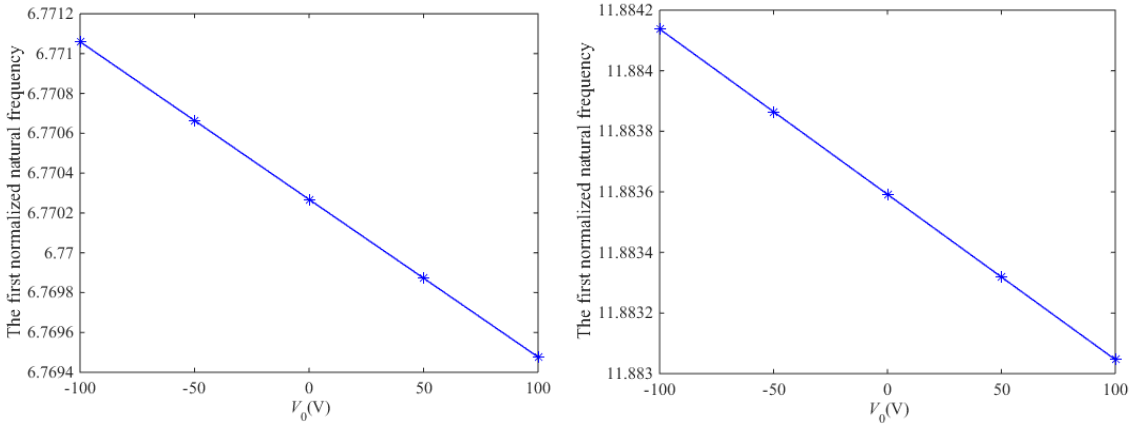


(a) SSSS (b) CCCC

*Fig. 3.* The impact of the parameter $V_0$ on the first non-dimensional frequency of the FGPP microplate (D-II, $a/h = 30, l/h = 0.2, e_0 = 0.2, K_w = 2, K_s = 0.1$)

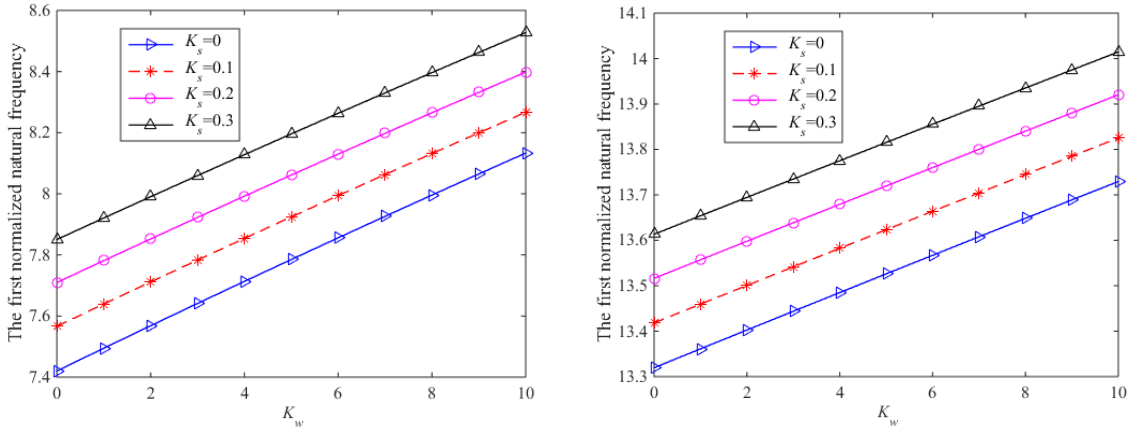


(a) SSSS (b) CCCC

*Fig. 4.* The influence of the spring coefficient on the lowest non-dimensional frequency of the FGPP microplate with various shear coefficients (D-III, $a/h = 20, l/h = 0.3, e_0 = 0.3, V_0 = 50$ V)

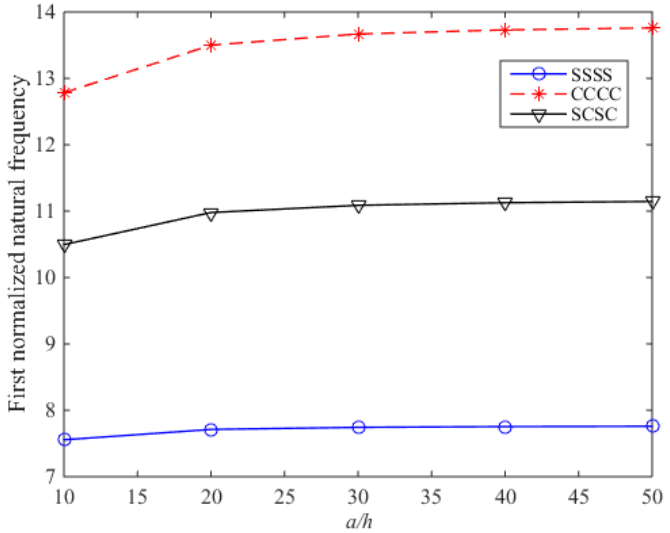


*Fig. 5.* The influence of the length-to-thickness ratio on the lowest non-dimensional frequency of the FGPP microplates (D-III, $l/h = 0.3, e_0 = 0.3, V_0 = 50$ V, $K_w = 2, K_s = 0.1$)

## 4. CONCLUSION

This study investigates the free vibration characteristics of the FGPP microplates with various porosity distributions using IGA combined with MSGT and HSDT. The governing equations are explicitly derived based on variational principles. The analysis focuses on the effects of porosity distribution, porosity coefficient, LSPs, external

electric voltage, and geometries on the natural frequencies of the FGPP microplates. The findings show that increasing the scale-to-thickness ratio leads to growth in the natural frequency. The stiffness of the FGPP microplates decreases as the porosity coefficient increases. The D-I distribution offers the highest stiffness among the examined porosity distributions, while the D-II distribution results in the lowest. Additionally, increasing the shear and spring parameters of the Winkler–Pasternak elastic foundation significantly raises the natural frequencies of the FGPP microplate. An increase in the initial electric voltage decreases the FGPP microplate's stiffness. The CCCC boundary condition yields the highest natural frequencies, whereas the SSSS condition results in the lowest values. Finally, an increase in the length-to-thickness ratio enhances the vibrational stiffness of the FGPP microplate. The results provide practical guidelines for tuning material gradation, porosity design, and electromechanical parameters to optimize the performance of FGPP microplate-based MEMS and microsystem devices.

## DECLARATION OF COMPETING INTEREST

The authors declare that they have no known competing financial interests or personal relationships that could have appeared to influence the work reported in this paper.

## ACKNOWLEDGMENT

This work was supported by to the project in 2025 funded by Ho Chi Minh City University of Technology and Education, Vietnam.

## REFERENCES

[1] D. C. C. Lam, F. Yang, A. C. M. Chong, J. Wang, and P. Tong. Experiments and theory in strain gradient elasticity. *Journal of the Mechanics and Physics of Solids*, **51**, (2003), pp. 1477–1508. https://doi.org/10.1016/s0022-5096(03)00053-x.

[2] T. T. Tran and D. K. Nguyen. Vibration of agglomerated CNTRC micro-scale beams carrying a moving concentrated load. *Vietnam Journal of Mechanics*, **46**, (2024), pp. 265–281. https://doi.org/10.15625/0866-7136/21064.

[3] B. Zhang, Y. He, D. Liu, L. Shen, and J. Lei. An efficient size-dependent plate theory for bending, buckling and free vibration analyses of functionally graded microplates resting on elastic foundation. *Applied Mathematical Modelling*, **39**, (2015), pp. 3814–3845. https://doi.org/10.1016/j.apm.2014.12.001.

[4] M. Kandaz and H. Dal. A comparative study of modified strain gradient theory and modified couple stress theory for gold microbeams. *Archive of Applied Mechanics*, **88**, (2018), pp. 2051–2070. https://doi.org/10.1007/s00419-018-1436-0.

[5] B. Wang, S. Zhou, J. Zhao, and X. Chen. A size-dependent Kirchhoff micro-plate model based on strain gradient elasticity theory. *European Journal of Mechanics - A/Solids*, **30**, (2011), pp. 517–524. https://doi.org/10.1016/j.euromechsol.2011.04.001.

[6] R. Ansari, M. F. Shojaei, V. Mohammadi, R. Gholami, and H. Rouhi. Size-dependent thermal buckling and postbuckling of functionally graded annular microplates based on the modified strain gradient theory. *Journal of Thermal Stresses*, **37**, (2014), pp. 174–201. https://doi.org/10.1080/01495739.2013.839767.

[7] R. Ansari, R. Gholami, M. Faghih Shojaei, V. Mohammadi, and S. Sahmani. Bending, buckling and free vibration analysis of size-dependent functionally graded circular/annular microplates based on the modified strain gradient elasticity theory. *European Journal of Mechanics - A/Solids*, **49**, (2015), pp. 251–267. https://doi.org/10.1016/j.euromechsol.2014.07.014.

[8] A. Karamanli and T. P. Vo. A quasi-3D theory for functionally graded porous microbeams based on the modified strain gradient theory. *Composite Structures*, **257**, (2021). https://doi.org/10.1016/j.compstruct.2020.113066.

[9] X.-H. Wu, C. Chen, Y.-P. Shen, and X.-G. Tian. A high order theory for functionally graded piezoelectric shells. *International Journal of Solids and Structures*, **39**, (2002), pp. 5325–5344. https://doi.org/10.1016/s0020-7683(02)00418-3.

[10] H. Tanzadeh and H. Amoushahi. Buckling and free vibration analysis of piezoelectric laminated composite plates using various plate deformation theories. *European Journal of Mechanics - A/Solids*, **74**, (2019), pp. 242–256. https://doi.org/10.1016/j.euromechsol.2018.11.013.

[11] X.-L. Huang and H.-S. Shen. Vibration and dynamic response of functionally graded plates with piezoelectric actuators in thermal environments. *Journal of Sound and Vibration*, **289**, (2006), pp. 25–53. https://doi.org/10.1016/j.jsv.2005.01.033.

[12] Z. Yan and L. Y. Jiang. Surface effects on the vibration and buckling of piezoelectric nanoplates. *EPL (Europhysics Letters)*, **99**, (2012). https://doi.org/10.1209/0295-5075/99/27007.

[13] Y. Tadi Beni. Size-dependent electromechanical bending, buckling, and free vibration analysis of functionally graded piezoelectric nanobeams. *Journal of Intelligent Material Systems and Structures*, **27**, (2016), pp. 2199–2215. https://doi.org/10.1177/1045389x15624798.

[14] Y. Ren and H. Qing. Elastic buckling and free vibration of functionally graded piezoelectric nanobeams using nonlocal integral models. *International Journal of Structural Stability and Dynamics*, **22**, (2022). https://doi.org/10.1142/s021945542250047x.

[15] F. Ebrahimi, A. Rastgoo, and M. N. Bahrami. Investigating the thermal environment effects on geometrically nonlinear vibration of smart functionally graded plates. *Journal of Mechanical Science and Technology*, **24**, (2010), pp. 775–791. https://doi.org/10.1007/s12206-010-0102-4.

[16] P. M. Phuc and N. T. Kim Khue. New finite modeling of free and forced vibration responses of piezoelectric FG plates resting on elastic foundations in thermal environments. *Shock and Vibration*, **2021**, (2021). https://doi.org/10.1155/2021/6672370.

[17] R. A. Ahmed, B. S. Khalaf, K. M. Raheef, R. M. Fenjan, and N. M. Faleh. Investigating dynamic response of nonlocal functionally graded porous piezoelectric plates in thermal environment. *Steel Compos Struct*, **40**, (2), (2021), pp. 243–54. https://doi.org/10.12989/scs.2021.40.2.243.

[18] W. Wang, H. Li, and L. Yao. Static bending and vibration analysis of a rectangular functionally gradient piezoelectric plate on an elastic foundation. *Applied Sciences*, **12**, (2022). https://doi.org/10.3390/app12031517.

[19] P. T. Dat, D. V. Thom, and D. T. Luat. Free vibration of functionally graded sandwich plates with stiffeners based on the third-order shear deformation theory. *Vietnam Journal of Mechanics*, **38**, (2016), pp. 103–122. https://doi.org/10.15625/0866-7136/38/2/6730.

[20] T. V. Lien and L. T. Ha. Dynamic analysis of functionally graded viscoelastic beams on the elastic foundation under multiple moving loads. *Vietnam Journal of Mechanics*, **47**, (2025), pp. 90–108. https://doi.org/10.15625/0866-7136/22165.

[21] T. T. Nguyen, H. N. H. Le, V. S. Lo, and T. T. Truong. Modal analysis of plates resting on elastic foundation based on the first-order shear deformation theory and finite element method. *Vietnam Journal of Mechanics*, **46**, (2024), pp. 354–366. https://doi.org/10.15625/0866-7136/21193.

[22] T. J. R. Hughes, J. A. Cottrell, and Y. Bazilevs. Isogeometric analysis: CAD, finite elements, NURBS, exact geometry and mesh refinement. *Computer Methods in Applied Mechanics and Engineering*, **194**, (2005), pp. 4135–4195. https://doi.org/10.1016/j.cma.2004.10.008.

[23] S. Thai, H.-T. Thai, T. P. Vo, and V. I. Patel. Size-dependant behaviour of functionally graded microplates based on the modified strain gradient elasticity theory and isogeometric analysis. *Computers & Structures*, **190**, (2017), pp. 219–241. https://doi.org/10.1016/j.compstruc.2017.05.014.

[24] C. H. Thai, A. J. M. Ferreira, and H. Nguyen-Xuan. Isogeometric analysis of size-dependent isotropic and sandwich functionally graded microplates based on modified strain gradient elasticity theory. *Composite Structures*, **192**, (2018), pp. 274–288. https://doi.org/10.1016/j.compstruct.2018.02.060.

[25] A. Farzam and B. Hassani. Size-dependent analysis of FG microplates with temperature-dependent material properties using modified strain gradient theory and isogeometric approach. *Composites Part B: Engineering*, **161**, (2019), pp. 150–168. https://doi.org/10.1016/j.compositesb.2018.10.028.

[26] P. T. Hung, P. Phung-Van, and C. H. Thai. A refined isogeometric plate analysis of porous metal foam microplates using modified strain gradient theory. *Composite Structures*, **289**, (2022). https://doi.org/10.1016/j.compstruct.2022.115467.

[27] I. J. Gibson and M. F. Ashby. The mechanics of three-dimensional cellular materials. *Proceedings of the Royal Society of London. A. Mathematical and Physical Sciences*, **382**, (1982), pp. 43–59. https://doi.org/10.1098/rspa.1982.0088.

[28] L.-L. Ke, Y.-S. Wang, J. Yang, and S. Kitipornchai. Free vibration of size-dependent magneto-electro-elastic nanoplates based on the nonlocal theory. *Acta Mechanica Sinica*, **30**, (2014), pp. 516–525. https://doi.org/10.1007/s10409-014-0072-3.

[29] M. R. Barati, H. Shahverdi, and A. M. Zenkour. Electro-mechanical vibration of smart piezoelectric FG plates with porosities according to a refined four-variable theory. *Mechanics of Advanced Materials and Structures*, **24**, (2017), pp. 987–998. https://doi.org/10.1080/15376494.2016.1196799.

[30] P. T. Hung, P. Phung-Van, and C. H. Thai. A refined isogeometric plate analysis of porous metal foam microplates using modified strain gradient theory. *Composite Structures*, **289**, (2022). https://doi.org/10.1016/j.compstruct.2022.115467.